Observations and Modeling of Rotational Signals in the *P* Coda: Constraints on Crustal Scattering

by N. D. Pham,[*] H. Igel, J. Wassermann, M. Käser, J. de la Puente, and U. Schreiber

Abstract In addition to three classical components (vertical, north–south, and east–west) of ground translations recorded by a broadband seismometer, a component of earthquake induced rotational ground motions around the vertical axis is consistently measured by a ring laser sensor located in Wettzell, southeast Germany. Significant rotations around the vertical axis in the *P* coda of teleseismic signals are either directly visible or can be inferred through the investigation of cross correlation between the transverse component (the component that is perpendicular to the great circle connecting the earthquake and the seismometer) of translation acceleration and ring laser rotation rate. Theoretically, in spherically symmetric isotropic media, we should not observe rotational signals around the vertical axis before the onset of *SH* waves. Possible causes for the observed rotations in the *P* coda are: (1) tilt–ring laser coupling, (2) anisotropy, (3) topographic scattering, and (4) *P-SH* scattering in the crust. Here we show that *P-SH* scattering in the 3D random crust can explain the observations and allow us to constrain crustal scattering properties.

Introduction

In seismology, observations are traditionally based on measurements of inertial seismometers that record three components (vertical, north–south, and east–west) of earthquake induced ground translations (displacement, velocity, or acceleration). There are theoretical studies suggesting that in addition to translations, rotational ground motions should be measured (e.g., Aki and Richards, 2002). This type of observation might be relevant for: (1) correcting translation signals recorded by classical seismometers for contamination by ground rotation (Graizer, 2005, 2006; Pillet and Virieux, 2007); (2) extracting additional information on earthquake source properties (e.g., Takeo and Ito, 1997; Takeo, 1998), soil—structure interactions (Trifunac and Todorovska, 2001) and properties of the subsurface (Igel *et al.*, 2007; Fichtner and Igel, 2009); and (3) providing additional ground-motion information to earthquake engineers for seismic design (e.g., Li *et al.*, 2001, 2002). However, the lack of instrumental resolution did not allow seismologists to record this kind of motion in a consistent way until recently (Pancha *et al.*, 2000; Igel *et al.*, 2005; Schreiber *et al.*, 2005; Cochard *et al.*, 2006; Igel *et al.*, 2007).

Ring laser technology has provided the means to allow, in principle, observation of rotational motions in a wide frequency band and epicentral distance range (Igel *et al.*, 2005;

Schreiber *et al.*, 2005; Igel *et al.*, 2007). The remarkable consistency between rotational ground motions around the vertical axis recorded by a ring laser and the transverse component (the component that is perpendicular to the great circle connecting the earthquake and seismometer) of translation acceleration (subsequently called transverse acceleration), for periods of 1 sec up to 150 sec and suitable values of the phase velocities estimated by taking the ratio of the transverse acceleration and vertical rotation rate, not only are proving the appropriateness of the ring laser sensor but also imply that the multicomponent observations allow the estimation of wave-field properties (e.g., phase velocities and propagation direction) that otherwise are only accessible with high accuracy through array measurements (Igel *et al.*, 2007).

In a previous study (Igel *et al.*, 2007), a significant rotational motion component around the vertical axis in the *P* coda of seismic signals had been recognized. At first, this is a surprising observation because, theoretically, in spherically symmetric isotropic media *P* and *SV* waves do not generate rotations around the vertical axis, so we should not observe this kind of motion before the arrival times of the *SH* waves. There are several possible explanations for the phenomenon of *P*-coda rotations: (1) tilt–ring laser coupling, when *P* waves arrive they do generate tilts at the Earth's surface (i.e., rotational motions around horizontal axes). This will contaminate the ring laser measurements

---

[*]Present address: Institute of Geophysics, Vietnamese Academy of Science and Technology, 18 Hoang Quoc Viet, Cau Giay, Hanoi, Vietnam

through changes of the surface normal with respect to the Earth's rotation axis and may potentially contribute to the phenomenon of rotation in the *P* coda (Schreiber *et al.*, 2005; Igel *et al.*, 2007). (2) *P-SH* scattering in the crust, (3) topographic scattering, and (4) anisotropy are additional possible explanations. The tilt–ring laser coupling is assumed to be small in the far-field case (McLeod *et al.*, 1998; Igel *et al.*, 2007). We detail and further systematically investigate this in a companion article (Pham *et al.*, 2009). In this study this effect is assumed negligible. The contributions of topographic scattering and anisotropy on the *P*-coda rotations are expected to be small but were never properly quantified. This will be the subject of a future study. Here, we focus on investigating the effects of *P-SH* scattering in the crust on rotational ground motions around the vertical axis.

The main goals of this study are to present the observations of rotational motions around the vertical axis in the *P* coda and to model these observations with 3D wave propagation through random crustal media.

Observations

Database

The data used in this study include collocated records of both the G-ring laser sensor and broadband seismometer (STS-2) at the Fundamental station, Wettzell, southeast Germany (see the Data and Resources section). The G-ring laser sensor is located in a purpose-built observatory and installed on a special material (to avoid effects of temperature, pressure, or deformation) and records rotational ground motions around a vertical axis. About 300 m away from this instrument, an STS-2 broadband sensor (WET station, latitude 49.15°, longitude 12.88°, German Regional Seismic Network) records permanently three orthogonal components of ground velocity. Further details on the instruments and the measurement principle can be found in Schreiber *et al.* (2006) and Igel *et al.* (2007).

Observations of 36 earthquakes that occurred between May 2003 and February 2008 are used in this study. The epicentral distance and magnitude distributions of the observed events are shown in Figure 1 with event information summarized in Table 1. Each event in this database includes four components recorded by the aforementioned instruments: three traditional components of ground velocity and one vertical component of ground rotation rate. Transverse acceleration, another component usually used in this study, is inferred by rotating (in a local radial-transverse system) the time-differentiated components of the observed horizontal ground velocities.

In the following we investigate the observed *P*-coda rotations systematically by examining their energy variations as a function of frequency, incoming direction, and time. The frequency and directional dependence of the *P*-coda rotations is revealed using the zero-phase Butterworth first-
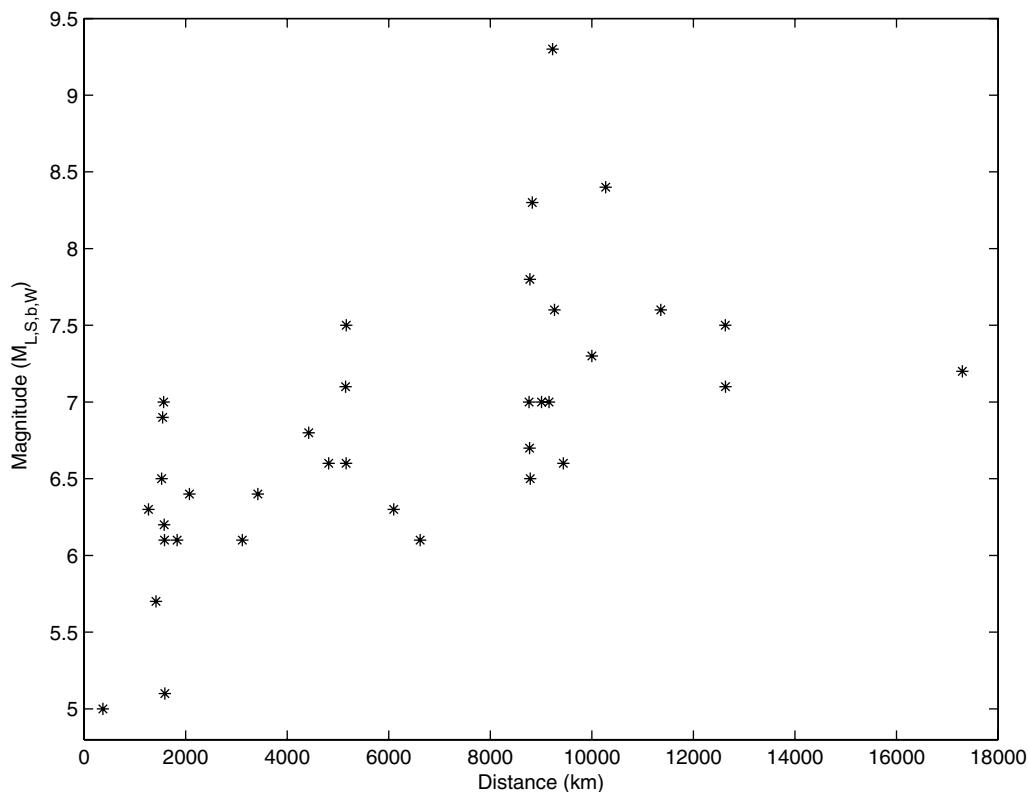

Figure 1.   Magnitude distribution of the observed events as a function of epicenter distance.

Table 1

Earthquakes Used in This Study

Date (mm/dd/yy)	Magnitude (L,b,S,W)	Latitude (°)	Longitude (°)	Depth (km)	Region	Distance (km)	Back Azimuth (°)	Note for Rotation Rate in the P Coda
05/21/03	6.9	36.96	3.63	12	Algeria	1547.2	212.3	Visible
05/26/03	7.0	38.85	141.57	68	Honshu	9009.2	38.0	Visible
07/06/03	5.7	40.44	26.02	17	Turkey	1415.1	128.2	Invisible
08/14/03	6.3	39.16	20.60	10	Greece	1268.6	148.2	Visible
09/25/03	8.1	41.80	143.91	27	Tokachi-oki	8828.0	34.9	Visible
09/27/03	7.5	50.04	87.81	16	Russia	5164.8	58.8	Visible
09/27/03	6.6	50.09	87.76	10	Russia	5158.9	58.8	Invisible
10/01/03	7.1	50.21	87.72	10	Siberia	5149.9	58.7	Invisible
10/08/03	6.7	42.65	144.57	32	Hokkaido	8773.3	34.0	Invisible
10/31/03	7.0	37.81	142.62	10	Honshu	9155.4	37.8	Invisible
11/17/03	7.8	51.15	178.65	33	Rat Islands	8780.6	9.0	Invisible
12/26/03	6.8	29.00	58.31	10	Iran	4426.5	103.3	Invisible
02/05/04	7.1	−3.62	135.54	16	Irian-Jaya	12629.5	66.5	Invisible
02/07/04	7.5	−4.00	135.02	10	Irian-Jaya	12628.5	67.2	Invisible
02/24/04	6.3	35.20	−4.00	0	Al Hoceima	2074.0	227.9	Invisible
03/17/04	6.1	34.59	23.33	24	Greece	1831.7	148.2	Invisible
04/05/04	6.6	36.51	71.03	187	Afghanistan	4817.6	84.3	Invisible
05/28/04	6.4	36.29	51.61	17	Iran	3424.5	100.0	Invisible
05/29/04	6.6	34.25	141.41	16	Honshu	9440.2	40.5	Invisible
12/05/04	5.0	48.12	8.08	10	Germany	370.8	253.8	Visible
12/26/04	9.3	3.30	95.98	30	Sumatra	9228.4	93.1	Visible
09/12/07	8.4	−4.44	101.37	34	Sumatra	10271.0	94.0	Visible
10/31/07	6.5	51.37	−178.38	28	Mariana Isl.	8787.0	352.9	Visible
11/14/07	7.6	−22.23	−69.91	40	North Chile	11356.0	249.9	Visible
12/09/07	7.2	−26.06	−177.52	190	South Fiji	17296.0	336.9	Visible
12/19/07	7.0	51.50	−179.50	60	Alentia	8763.0	352.2	Invisible
01/06/08	6.5	37.40	22.70	70	South Greece	1526.0	145.2	Visible
01/09/08	6.3	32.70	85.20	50	Xizang	6098.6	78.7	Invisible
02/08/08	6.1	11.00	−42.70	10	Atlantic	6617.8	250.0	Visible
02/14/08	7.0	36.60	21.70	30	Greece	1566.7	149.6	Visible
02/14/08	6.1	36.50	21.90	33	Greece	1584.2	149.2	Visible
02/19/08	5.1	36.40	21.80	40	Greece	1590.6	149.7	Invisible
02/20/08	7.6	2.90	96.00	33	Sumatra	9263.6	93.3	Invisible
02/20/08	6.2	36.50	21.70	25	Greece	1576.8	149.8	Visible
02/21/08	6.1	77.10	18.40	10	Svalbard	3117.7	2.6	Invisible
02/25/08	7.3	−2.50	99.90	33	Sumatra	10001.0	93.9	Invisible

order filtering and cross-correlation techniques. Normalized envelopes are used to investigate time-dependent variations of energy in the *P*-coda rotations.

Frequency Dependence of Direct Observations

Analysis of the observed data showed that the rotational signals around the vertical axis are visible in the *P*-coda sections of strong (or near) earthquakes. A typical example for these direct observations is the case of the 12 September 2007 *M* 8.4 Sumatra earthquake. To examine the frequency dependence of the *P*-coda rotations, we low-pass filter the signals with different cutoff periods. The results are shown in Figure 2. We observe that with increasing cutoff period, the amplitude of the *P*-coda rotations is decreased. Amplitudes of the *P*-coda rotational signals decrease significantly for a cutoff period $T = 5$ sec and almost disappear when the cutoff period reaches a value of 10 sec. This implies that the energy of the observed *P*-coda rotations is predominant at

high frequencies. This phenomenon is observed for all events with visible *P*-coda rotations.

Increase in Correlation Right After the Onset of *P* Wave

As indicated in Table 1, in many cases rotational energy in the *P* coda is hidden in the noise. An example is shown in Figure 3. The 24 February 2004 *M* 6.4 Al Hoceima event does not show visible *P*-coda rotations (Fig. 3, the third trace from the top). To investigate the variation of rotation rate in such events, we use the cross-correlation technique. Theoretically, assuming plane shear-wave propagation in the horizontal direction with transverse polarization, the vertical rotation rate and transverse acceleration should have the same waveform, and their amplitudes should scale proportionally to two times the phase velocity (Igel *et al.*, 2005; Cochard *et al.*, 2006; Igel *et al.*, 2007). In the *P*-coda time window, with clear visibility of transverse acceleration, an
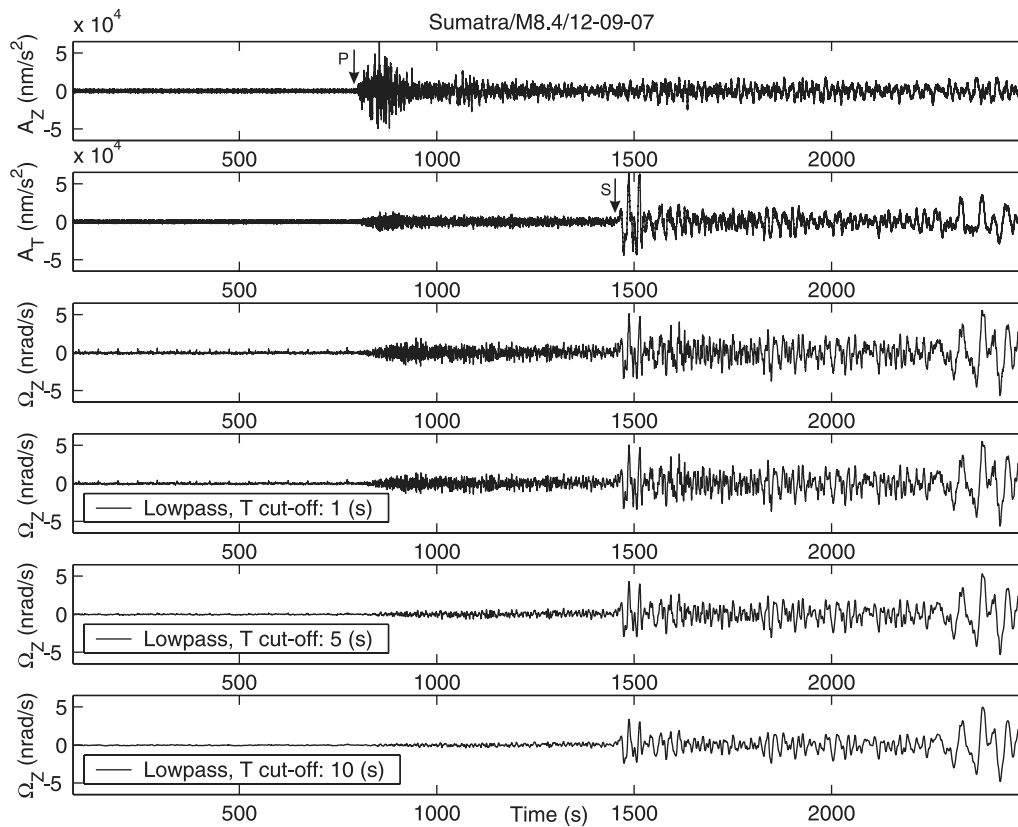
Figure 2.   Observations of translation and rotational ground motions induced by the 12 September 2007 M 8.4 Sumatra earthquake. Top three traces: unfiltered vertical and transverse components of ground acceleration and rotation rate, respectively. Bottom three traces: lowpass filtered rotation rate with cut off periods 1, 5, and 10 sec, respectively. Significant energy of rotational motions in the P coda is visible and predominant at high frequencies.

increase of correlation between rotation rate and transverse acceleration would therefore indicate the presence of (scattered) SH energy because (as mentioned before) P and SV waves do not generate rotations around the vertical axis. The zero-lag normalized cross-correlation coefficient—defined between zero (no similarity) and one (perfect match)—between vertical rotation rate and transverse acceleration was calculated for a sliding time window of appropriate length (twice the dominant period) along the time series. After high-pass filtering both signals (transverse acceleration and rotation rate) with cutoff period $T = 1$ sec, using a 2 sec sliding time window, the results reveal a clear increase of the coefficients right after the onset of P (Fig. 3, bottom panel). The same processing for all events in the period 2003–2004 shows a clear increase of the correlation coefficients between the high-pass filtered rotation rate and high-pass filtered transverse acceleration at (and following) the onset of P waves for all events (Fig. 4). This result indicates the existence of high-frequency P-coda rotations for all events, sometimes hidden in the noise.

In order to quantify and document the observations systematically, we focus on four earthquakes with visible P-coda rotations (signal-to-noise ratio [S/N] ≥ 1.86). Their

magnitudes, epicenter distances, and back azimuths are given in Table 2.

Frequency Dependence of Correlation

One of the expectations of ring laser measurements is to help seismologists separating P and S waves in the wave field (e.g., Takeo and Ito, 1997). The appearance of P-coda rotations seems to frustrate that hope. Because the dominant periods of directly arriving energy of P and S waves are different, we investigate the cross correlation between high-pass filtered transverse acceleration and vertical rotation rate as a function of time and cutoff period. Sliding window lengths were taken twice as long as the cutoff periods. The cutoff period range was chosen large enough to cover at least the dominant periods of the directly arriving P energy (around 1 sec) and S energy (around 5 sec). Typical results are shown in Figure 5a,b (see also Igel *et al.*, 2007). At the bottom subplots, the zero-lag normalized cross-correlation coefficients as a function of time and cutoff period are presented in the same window as the seismograms. At high frequencies, we can see a sharp increase in correlation at and following the direct P wave (subplot four from the top and the bottom
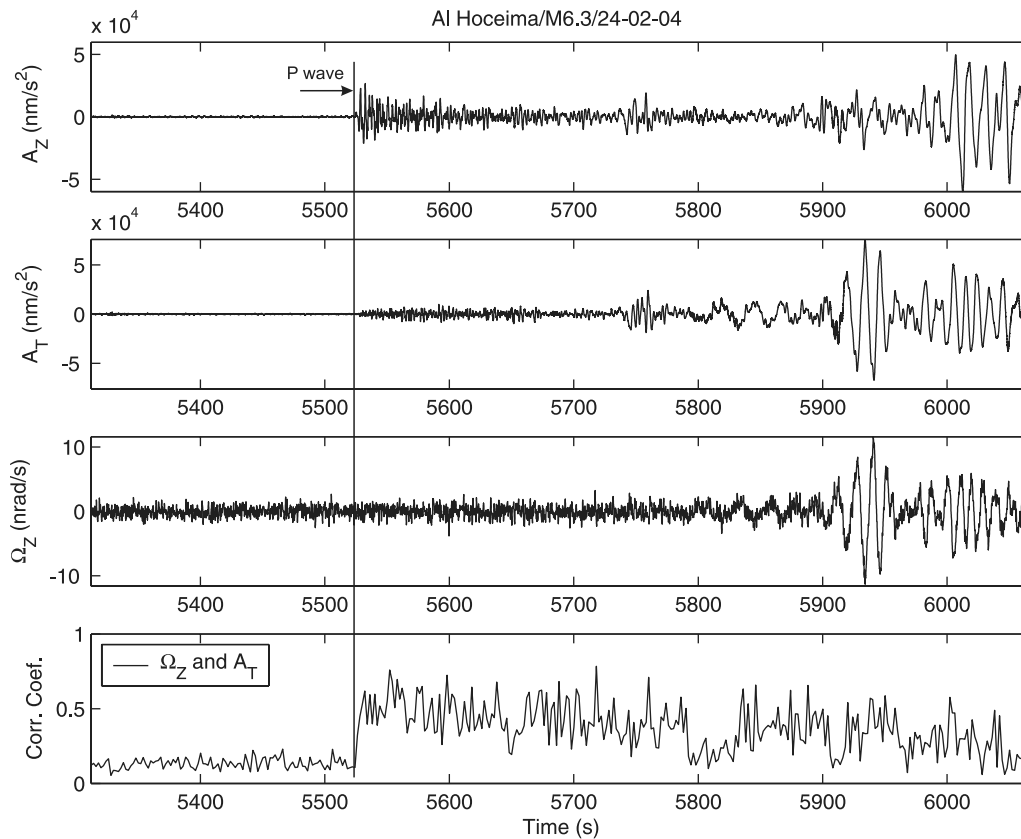
Figure 3.   Top three traces: vertical and transverse accelerations and rotation rate, respectively, for the 24 February 2004 *M* 6.4 Al Hoceima event. Bottom panel: zero-lag normalized cross-correlation coefficients between rotation rate and transverse acceleration calculated for 2 sec sliding time windows (after high-pass filtering with a cutoff period of 1 sec).

panel). This correlation smears out and becomes less pronounced with increasing period, while the corresponding correlation of *SH*- and Love-wave type signals increases with the period. It is interesting to note the distinct increase of correlation at specific arrival times. This may well indicate specific seismic phases (shear waves, *P-S* conversions).

Directional Dependence of Correlation

So far, the translation data were rotated into transverse and radial components according to the theoretical back azimuth derived from known coordinates of the earthquake epicenter and observation station. But—as shown in Igel *et al.* (2007)—the cross correlation is highly azimuth dependant. For *S* and Love waves it allows estimating back azimuth. In the *P* coda it may give hints as to where the *SH* energy comes from. To investigate this further the directional dependence of the correlation between horizontal acceleration and rotation rate is examined in detail.

We calculate horizontal acceleration with assumed back azimuths varying in the range of 0°–360° then examine the zero-lag normalized cross-correlation coefficients between horizontal acceleration and rotation rate in sliding time windows. High-pass filters with appropriate cutoff periods were applied before correlating. Sliding window lengths were

taken twice as long as the cutoff periods. Figure 6 shows typical results for the case of the Tokachi-oki event. In the fifth subplot (from the top) and the bottom panel of this figure, the correlation coefficients as a function of time and assumed back azimuth are shown in the same time window. In the fourth and the fifth subplots the cutoff period $T = 5$ sec and sliding window length 10 sec were used. High-correlation coefficients are distributed around the theoretical back azimuth (indicated by a horizontal black line) at the onset times of *SH* and Love waves. When the cutoff period $T = 1$ sec and sliding window length 2 sec were used (bottom two subplots), we observe at the bottom of this figure that high-correlation coefficients are more evenly distributed with angle in the *P* coda, suggesting that the rotational energy comes from all directions.

To estimate the back azimuth at longer periods, we sum up over time the correlation coefficients that were calculated with cutoff periods $T \geq 5$ sec (dominant period of directly arriving *S* wave) over a window containing *SH* and Love waves. The estimated back azimuth is associated with the maximum of the sum. In Figure 7, the distribution of the normalized sums as a function of assumed back azimuth are shown for four typical events (Algeria, 21 May 2003 *M* 6.9; Russia, 27 September 2003 *M* 7.5; Tokachi-oki, 25 September 2003 *M* 8.1; Sumatra, 12 September 2007 *M* 8.4). For all
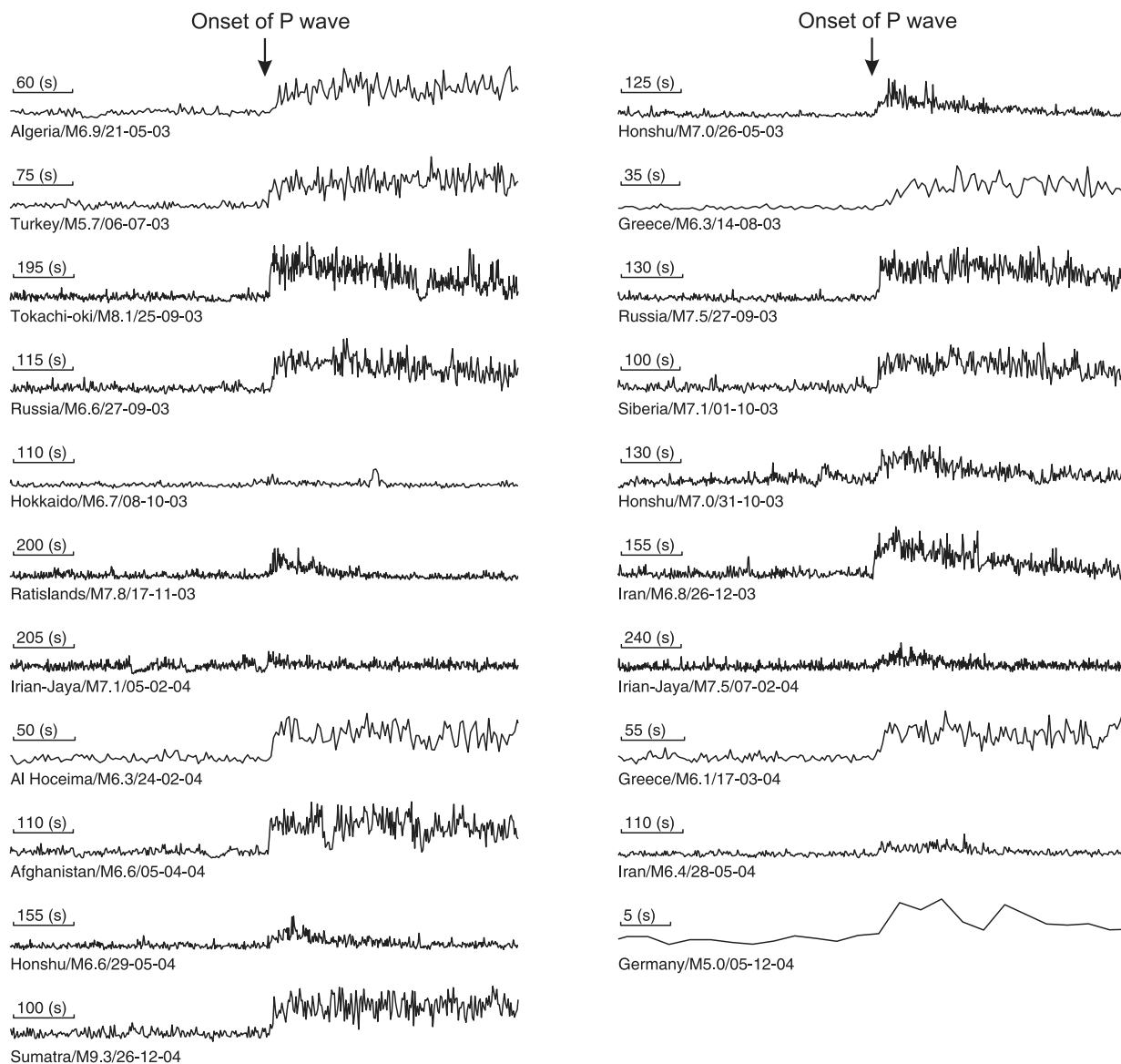
Figure 4. Zero-lag normalized cross-correlation coefficients between rotation rate and transverse acceleration in 2 sec sliding time windows (after high-pass filtering with a cutoff period of 1 sec) calculated for 21 events observed in 2003–2004. The correlation coefficients increase at and following the onset of *P* waves in all of these observed events.

these events, there exist clear maxima. The theoretical back azimuths indicated by horizontal black lines correspond almost exactly to the peaks of the normalized sums. The estimated and theoretical back azimuths, respectively, are 223° and 212° (Algeria event), 63° and 59° (Russia event), 38° and 35° (Tokachi-oki event), and 86° and 94° (Sumatra event). The difference can be explained by the influence of 3D structure on the propagation direction or the nonplanarity

Table 2
Earthquakes Studied in Detail

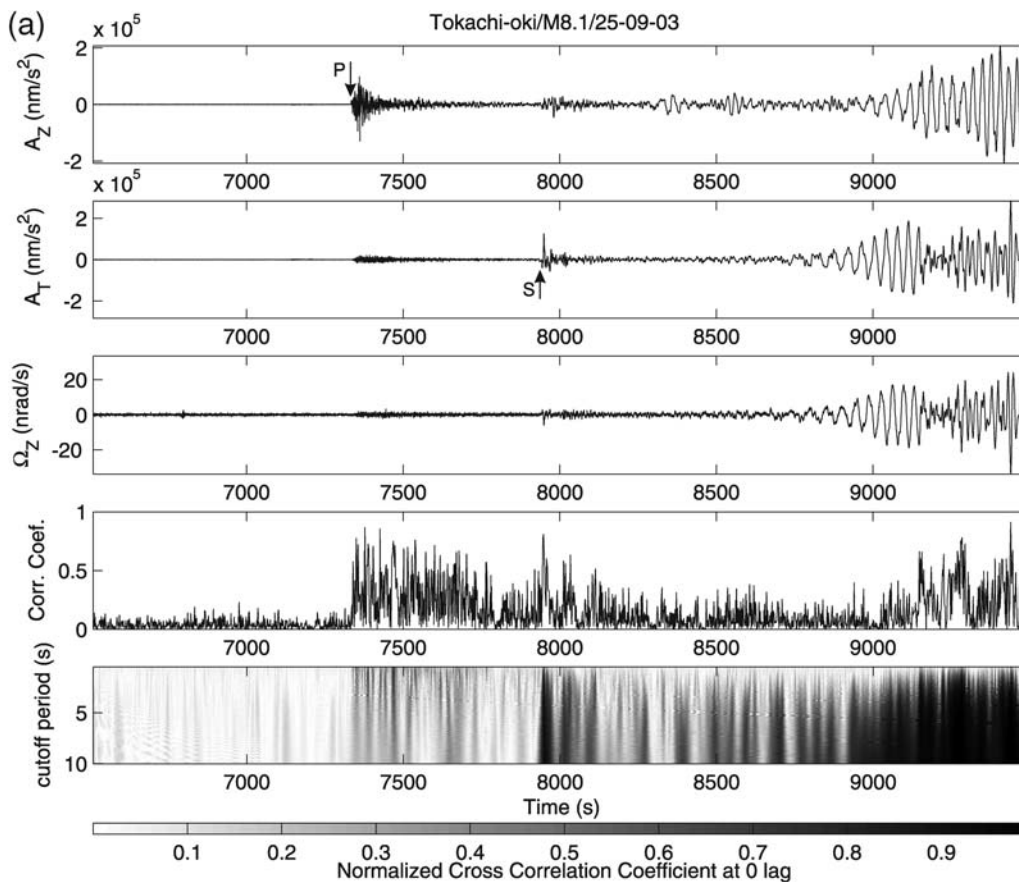| Date (mm/dd/yy)	Magnitude (L,b,S,W)	Latitude (°)	Longitude (°)	Depth (km)	Region	Distance (km)	Back Azimuth (°)	S/N (*P* coda)	
								V_z	Ω_z
05/21/03	6.9	36.96	3.63	12	Algeria	1547.2	212.3	158.18	2.53
09/25/03	8.1	41.80	143.91	27	Tokachi-oki	8828.0	34.9	359.82	2.75
09/27/03	7.5	50.04	87.81	16	Russia	5164.8	58.8	143.24	1.86
09/12/07	8.4	−4.44	101.37	34	Sumatra	10271.0	94.0	58.60	2.93

Figure 5. (a) Top three traces: vertical and transverse accelerations and rotation rate, respectively, for the 25 May 2003 *M* 8.1 Tokachi-oki event. The fourth trace (from the top): the zero-lag normalized cross-correlation coefficients between rotation rate and transverse acceleration after high-pass filtering with a cutoff period of 1 sec, calculated for 2 sec sliding time windows. Bottom panel: the correlation coefficients as a function of time and cutoff period (length of the sliding time window is twice as long as the high-pass cutoff period). (b) Top three traces: vertical and transverse accelerations and rotation rate, respectively, for the 12 September 2007 *M* 8.4 Sumatra event. The fourth trace (from the top): the zero-lag normalized cross-correlation coefficients between rotation rate and transverse acceleration after high-pass filtering with a cutoff period of 1 sec, calculated for 2 sec sliding time windows. Bottom panel: the correlation coefficients as a function of time and cutoff period (length of the sliding time window is twice as long as the high-pass cutoff period). (*Continued*)

of the wavefronts. This processing can be used to estimate the direction of the incoming seismic transversely polarized wave field.

To investigate the direction of the incoming energy of *P*-coda rotations, we examine the distribution of the same normalized sums over the window of the *P* coda for cases with cutoff periods $T \leq 2$ sec (around the dominant period of directly arriving *P* wave). The results are shown in Figure 8. The normalized sums in the *P* coda have almost even distributions with angle for all four events. This result implies that energies of high-frequency rotational motions about a vertical axis in the *P* coda come from many different directions, indicative of a strongly scattered wave field.

Envelopes

As mentioned previously, tilt-ring laser coupling or scattering may contribute to the *P*-coda rotations. If tilt-ring laser coupling strongly contributes to the observations, energies of

the *P*-coda rotations should appear right after the onset of *P* waves. Therefore, we investigate in the following the time-dependent variation of energies of observed translation and rotational seismograms in the *P* coda.

In seismology, the envelope of a time series is an unsigned low pass of the original signal. It shows the time-dependent variation of amplitudes (or energies) of the time series. The normalization erases any influence of polarities in order to ease recognition of similarities or differences in the waveforms. However, relative amplitudes within the trace are preserved.

The normalized envelope Y of a seismogram X is defined as

$$Y(t) = \frac{\text{abs}[X(t)] + j^* H[X(t)]}{\max\{\text{abs}[X(t)] + j^* H[X(t)]\}}.$$

In this definition j is the imaginary unit, and H represents the Hilbert transform of time series X.
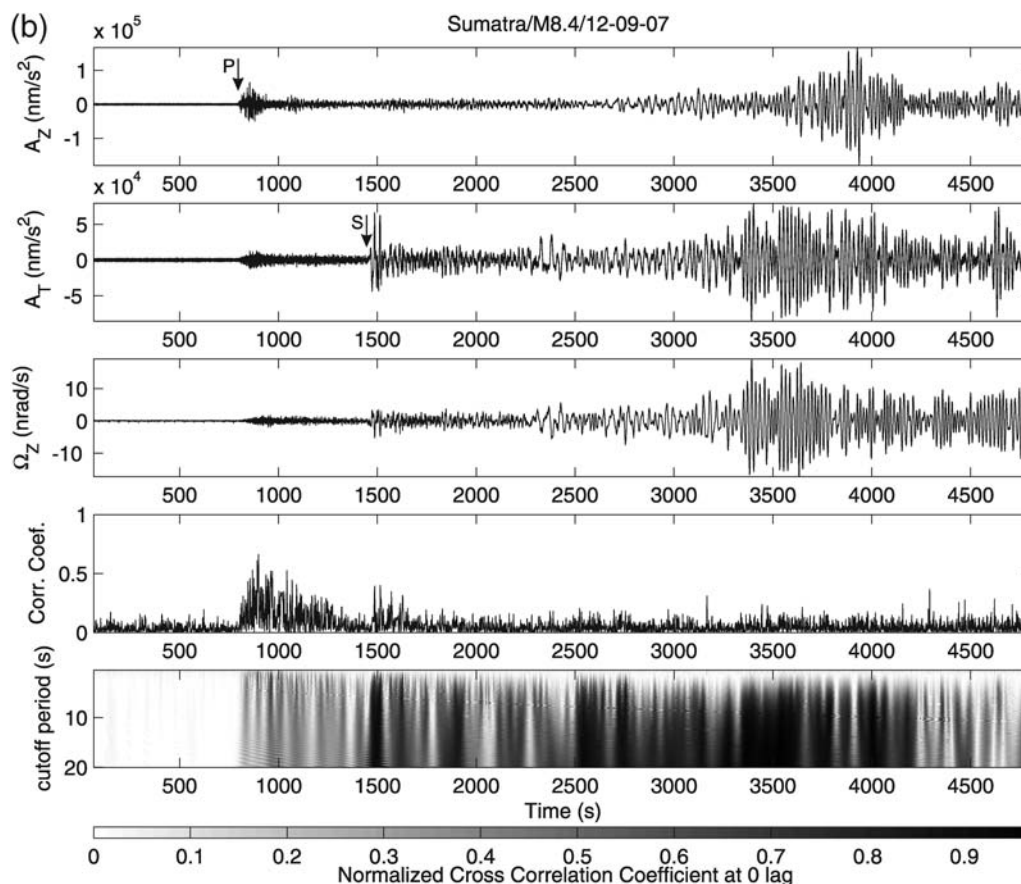
Figure 5. Continued.

The normalized envelopes of rotation rate and the vertical and transverse components of ground velocities are calculated. The results for four earthquakes are shown in Figure 9. In each subplot (from the top, respectively) individually normalized envelopes of vertical velocities, transverse velocities, rotation rate, superposition of the envelopes of vertical and transverse velocities, and superposition of vertical velocity and rotation rate of each event are shown. We can recognize that the amplitude of vertical velocity (the top trace) increases very fast right after the *P*-wave onset. Whereas, after the arrival time of the direct *P* wave, the amplitude increase of transverse velocity and rotation rate is delayed (the second and third traces from the top and the two bottom traces). However, the increases of transverse velocity and rotation rate amplitudes remain even though the amplitude of vertical velocity passes its maximum value and decreases.

Before proceeding to model aspects of these observations, we can summarize that the energies of the observed *P*-coda rotations are predominant at high frequencies, come from many different directions, and increase with time slower than that of the direct *P* waves. These results suggest that *P-SH* scattering is the dominant cause for the observations. We proceed to quantify these observations by

modeling complete six-component seismograms in 3D random media.

Modeling

Scattering is a phenomenon generated by the interaction between primary waves and inhomogeneities. In this process the amplitudes of the primary seismic waves are reduced as they propagate, but the energy of the propagating wave field is conserved. As mentioned by Stein and Wysession (2003), this process can be described by elastic wave theory in which the governing parameters are: (1) the wavelength of the wave field (or the wavenumber), (2) the distance that the wave travels through the heterogeneous region, (3) the heterogeneity size, and (4) the velocity perturbation. When the size of the velocity heterogeneities is close to the wavelength of the wave field and the travel distance is large enough compared to the wavelength, scattered energy is predominant (Aki and Richards, 2002; Stein and Wysession, 2003). Random media can be generated for desired correlation lengths and velocity perturbations (e.g., Klimeš, 2002).

The purpose of the forward modeling in this section is to study the generation of *P*-coda rotations under the assumption of *P-SH* scattering in the crust. Thus, any other contribution to the *P*-coda rotations except *P-SH* scattering needs
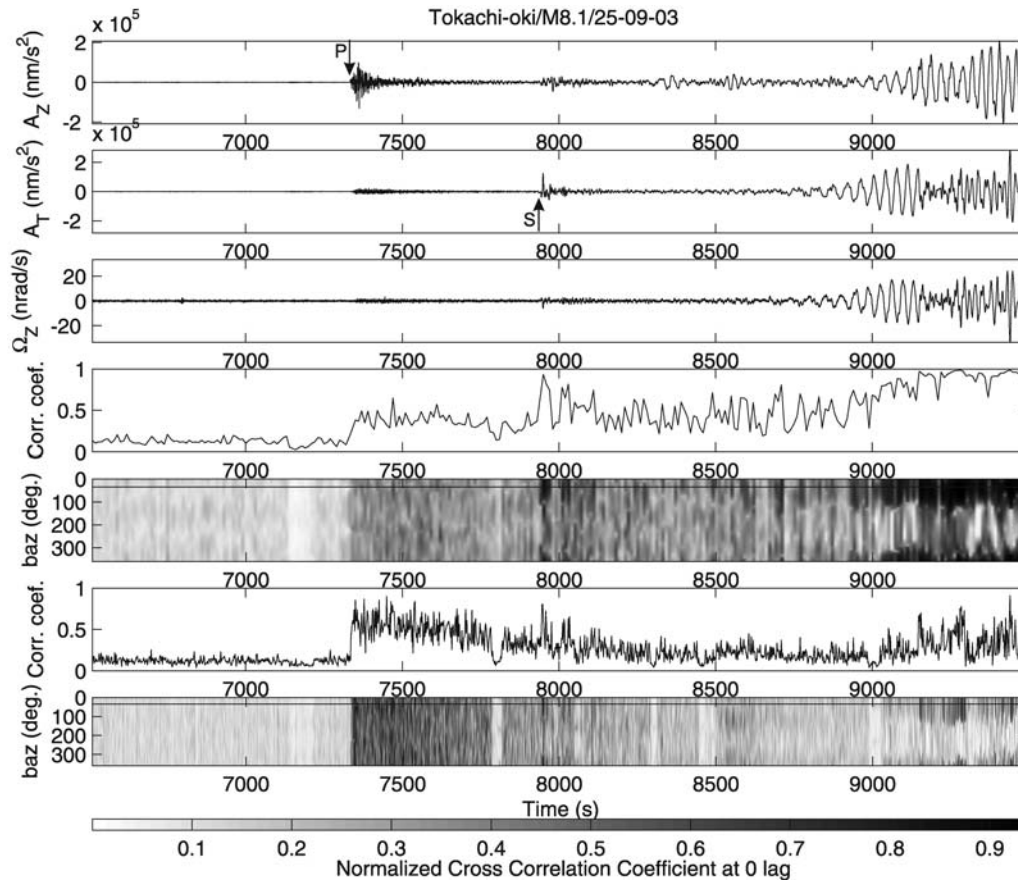
Figure 6. Top three traces: vertical and transverse accelerations and rotation rate, respectively, for the 25 September 2003 *M* 8.1 Tokachi-oki event. The fourth and sixth traces (from the top): the zero-lag normalized cross-correlation coefficients between rotation rate and transverse acceleration after high-pass filtering with cutoff periods of 5 and 1 sec, calculated for 10 and 2 sec sliding time windows, respectively. The fifth and bottom panels: the correlation coefficients as a function of time and assumed back azimuth (high-pass filter with cutoff periods of 5 and 1 sec and sliding time windows of 10 and 2 sec were applied, respectively). The theoretical back azimuth is indicated by a horizontal line.

to be avoided. To satisfy this, we model complete theoretical seismograms created by a plane *P* wave of dominant period 1 sec (the same as the predominant period of the observed *P* waves), propagating upward in the vertical direction from the bottom of a random medium.

A random medium can be described through a spatial distribution $u(x)$ of material parameters u. This distribution can be expressed as (Klimeš, 2002)

$$u(x) = u_0(x) + U(x),$$

where $u_0(x)$ is the mean value of $u(x)$, and $U(x)$ is a realization of the random quantity. In our study, to simplify the modeling, we perform simulations with random media in which the wave velocities are randomly perturbed in space, but the mass density ρ, the ratio between *P*- and *S*-wave velocities V_P/V_S, and the mean values of the velocities are kept constant. The realization of the random velocities is calculated in terms of white noise filtered by a spectral filter (see Klimeš, 2002). Because we just consider high frequencies (i.e., small heterogeneities), we choose the spectral filter cor-

responding to the Zero Von Kármán correlation function mentioned in Klimeš (2002):

$$\hat{f}(k) = \kappa(a^{-2} + k^2)^{-d/4},$$

where a is the Von Kármán correlation length, d is the Euclidean dimension of the space, and κ is a constant corresponding to the given value of perturbation.

To be as realistic as possible, the used model setup is based on the crust model of Bassin *et al.* (2000) at the Wettzell area. The model is 60,800 m long, 60,800 m wide, and 40,850 m deep. The mass density is taken as $\rho = 2.9$ g/cm³, and the mean values of the *P*- and *S*-wave velocities, respectively, are $V_P = 6600$ m/sec and $V_S = 3700$ m/sec. In order to produce significant scattering energy, we use correlation lengths between 1000 and 15,000 m (see Aki and Richards, 2002; Stein and Wysession, 2003). Furthermore, the root mean square perturbation of the wave velocities is taken in the range from 0% (homogeneity) up to about 11%.
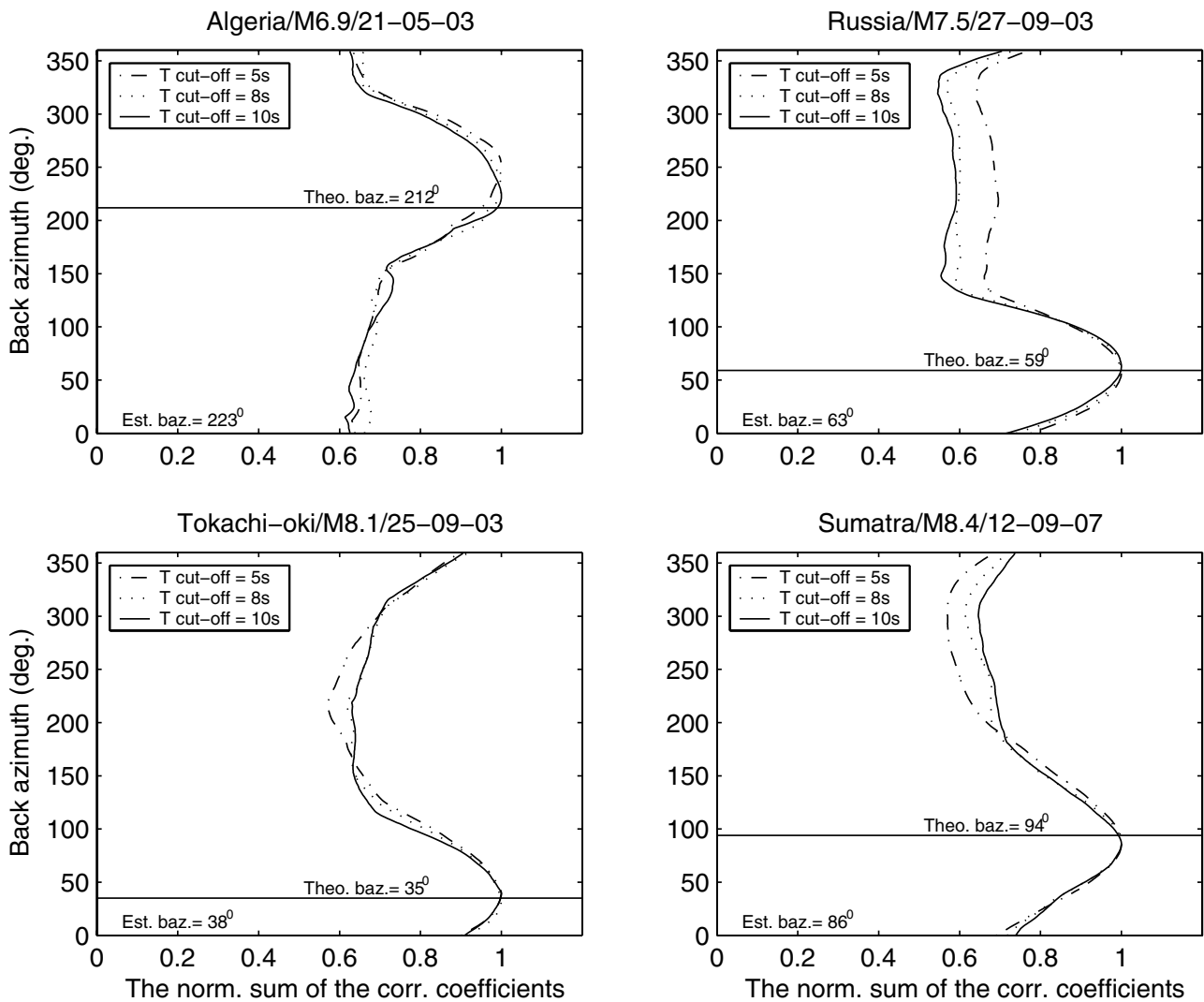
Figure 7. Distribution of the (normalized) sum of the correlation coefficients (between rotation rate and transverse acceleration after high-pass filtering with cutoff periods of 5, 8, and 10 s, length of sliding time window is twice as long as the cutoff period applied before correlating) in the window containing direct *SH* and Love waves of several observed events as a function of assumed back azimuth.

Seismograms are calculated using the ADER-DG method (the combination of a Discontinuous Galerkin finite element method and an Arbitrary high-order DERivative time integration approach developed by Dumbser and Käser [2006]) that was extended to allow outputting the three components of rotation rate, in addition to the three components of translational velocity. The modeling parameters are detailed in Table 3.

Figure 10 illustrates schematically a 3D Von Kármán random medium used in this study with correlation length $a = 2000$ m, root mean square perturbation of 6.51%. In addition, synthetic seismograms obtained at three receivers located at different sites on the surface of the model are shown. For each set of translational velocities (V_x, V_y, and V_z) or rotation rates (Ω_x, Ω_y, and Ω_z) the amplitudes are scaled. The figure shows that, as waves travel through the random medium, both rotational and horizontal translation components are generated by scattering. The delayed arrival of the

vertical rotation compared to the onset of the vertical velocity that we noticed in the observations can also be clearly seen in our synthetics. Moreover, the simulated seismograms differ at each station because the random field is completely 3D. This allows us to stack aspects of the data from different receivers rather than multiple simulations.

To systematically investigate the effects of the perturbation on *P*-coda rotations, we first fix the correlation length to 2000 m then calculate seismograms with different velocity perturbation amplitudes. Figure 11 shows the simulated seismograms obtained at the receiver located at the center of the model surface as a function of time and velocity perturbation. We can see that for a homogeneous medium (i.e., zero perturbation) no rotational or horizontal translations are generated. Energy in these components appears only in the case of random media. We can also observe that, as the velocity perturbation increases, the peak amplitudes of these signals increase, while the vertical velocity decreases.
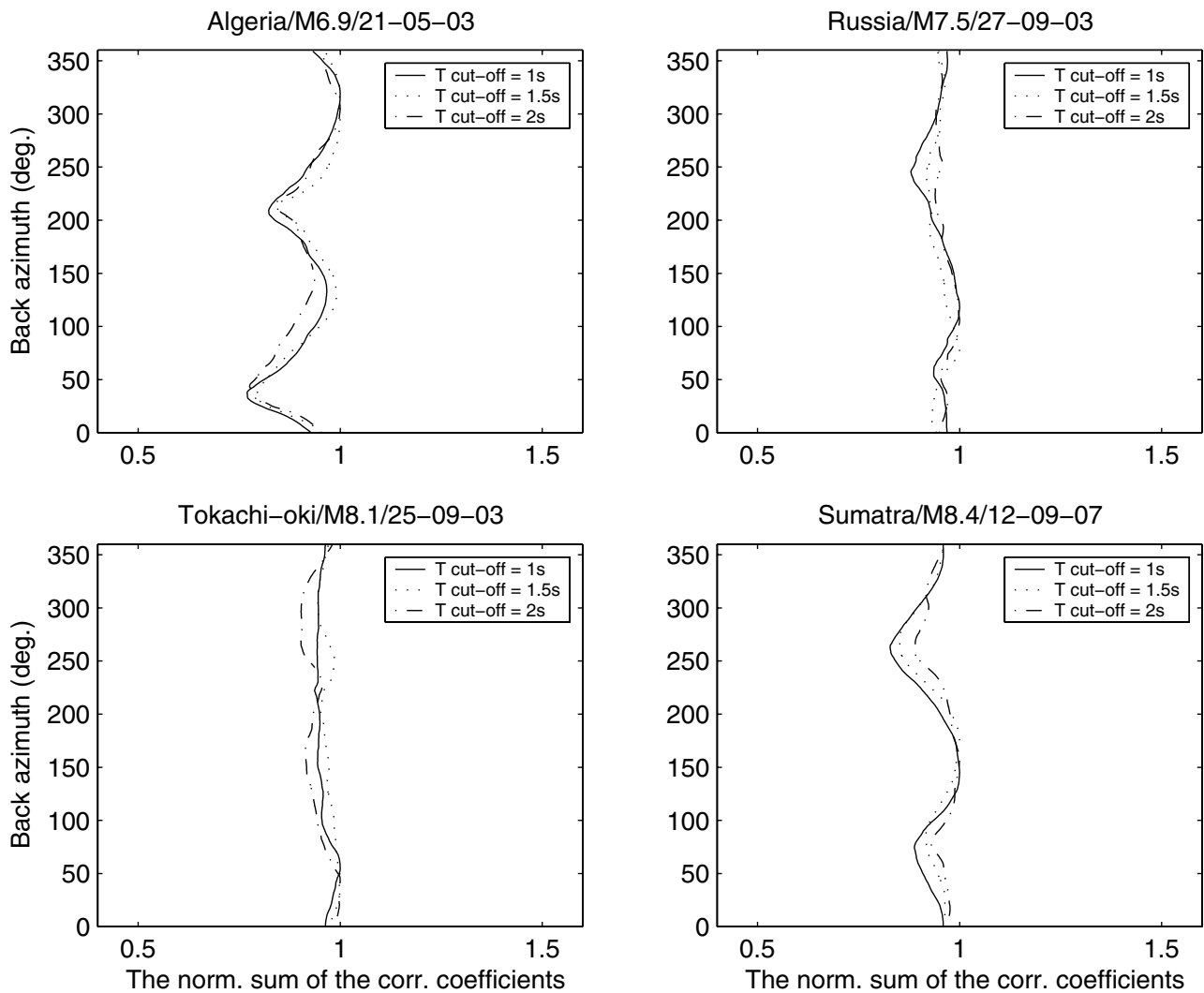
Figure 8. Distribution of the (normalized) sum of the correlation coefficients (between rotation rate and transverse acceleration after high-pass filtering with cutoff periods of 1, 1.5, and 2 s, length of sliding time window is twice as long as the cutoff period applied before correlating) in the *P*-coda window of several observed events as a function of back azimuth. The almost even distribution implies that high-frequency rotational energy in the *P* coda comes from all azimuthal directions.

The effects of scattering can be quantified by considering both the peak amplitudes and energy of all six components of motion at the surface. The energy representative, defined as the sum over the squared amplitude, will be referred to simply as "energy" in the following. More information on the concept of elastic wave energy density can be found in Hennino *et al.* (2001). Furthermore, because the media are random in all three dimensions, we perform an average of the peak amplitudes and energies computed at 24 receivers located around a circle of a radius 15,000 m on the surface of the model (see Fig. 10), taking the first 21 sec of each trace. In total, we investigate 10 different random models characterized by varying velocity perturbations.

The results shown in Figure 12 imply that part of the energy in the vertical component is scattered into energy of rotational and horizontal motions. This figure suggests that the ratio of energies of rotation rate and vertical velocity can

be used to characterize and eventually constrain scattering. Another result illustrated in Figure 12 is that the horizontal components of rotation rate (i.e., tilt) have generally higher amplitudes than the vertical ones.

The key question is: How can we compare the simulated *P*-coda rotation with the observed ones? We follow studies by Shapiro *et al.* (2000) and Hennino *et al.* (2001) who proposed using the ratio of energies of curl and divergence of ground motions to distinguish between the different scattering regimes in the lithosphere. Using the curl of the wave field derived from array-translation measurements, the authors showed that there is an energy equipartition, indicated by the stabilization of the energy ratio.

We first return to the observations and investigate the ratio of energies (i.e., sum of squared amplitudes) of the observed rotation rate (Ω_z) and vertical velocity (V_z) in sliding time windows from the onset of *P* waves along the *P* coda.
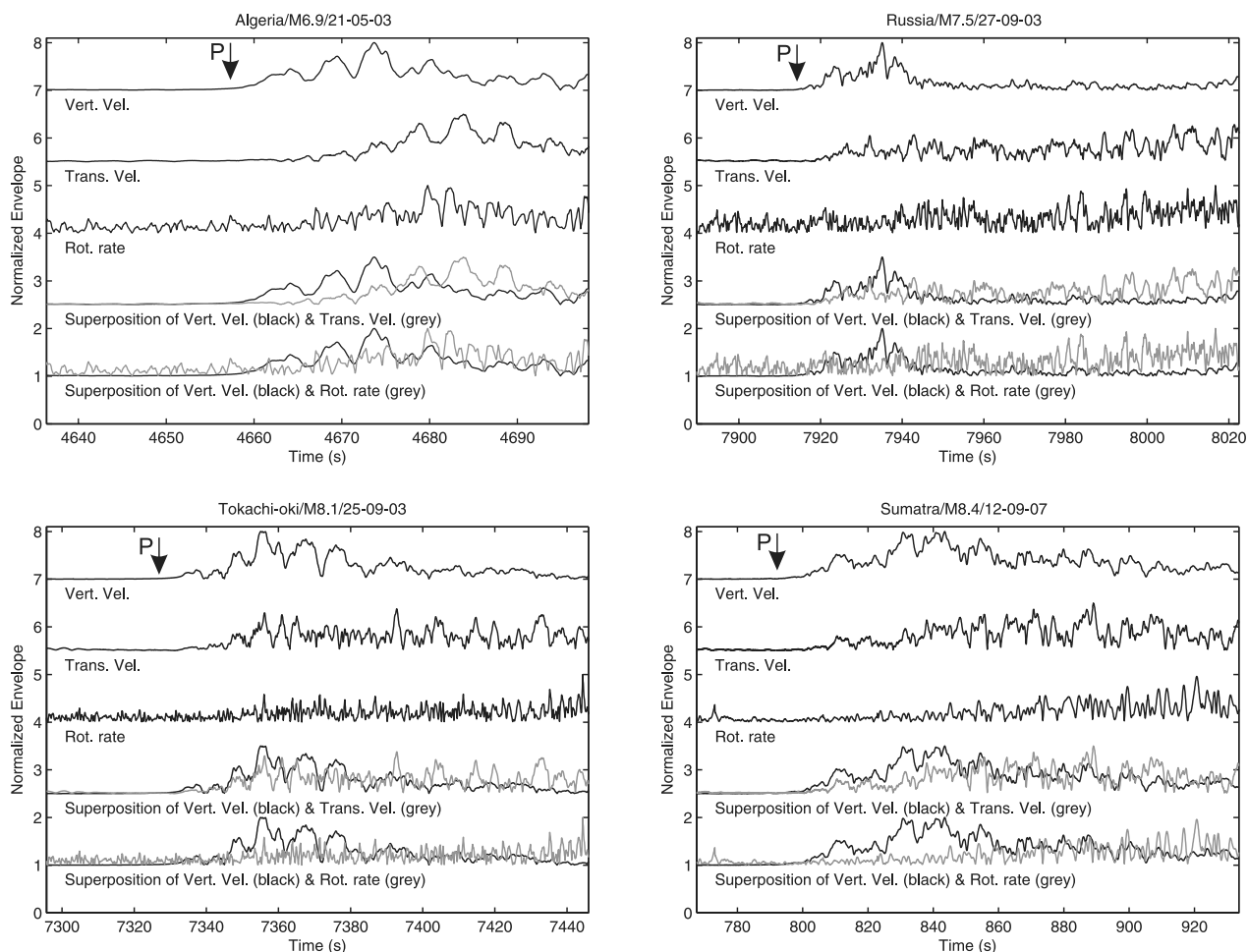
Figure 9. Normalized envelopes of individual seismograms and their superposition. For each subplot (from the top, respectively): normalized envelopes of vertical and transverse components of ground velocity, vertical component of rotation rate, and the superposition of the envelopes of vertical and transverse velocities, and superposition of vertical velocity and rotation rate.

The length of the sliding time windows was varied from 5 to 20 sec. Figure 13a shows a typical result for the case of the 12 September 2007 M 8.4 Sumatra earthquake. We observe that after the P arrival, the ratio is reduced (the third trace from the top, before 810 sec). After a short time of decrease, the energy ratio is quite stable until the energy of V_z reaches the maximum value (the section between 810 and 860 sec). Then the energy ratio starts increasing because the amplitude of V_z is decreased while that of Ω_z is still increasing (the

section between 86 and 965 sec). The ratio reaches the peak value when the energy of Ω_z in the sliding time window reaches the maximum value. Zooming in the ratio in the section between 800 and 875 sec (bottom panel), we can see that for cases of window lengths 15 and 20 sec the ratios have a stable value of about 1×10^{-8}. For smaller window lengths (5 and 10 sec) the ratios vary around this value. For the case of the 25 September 2003 M 8.1 Tokachi-oki earthquake, we obtain the same result with the stable value of the energy

Table 3
Modeling Parameters Used in This Study

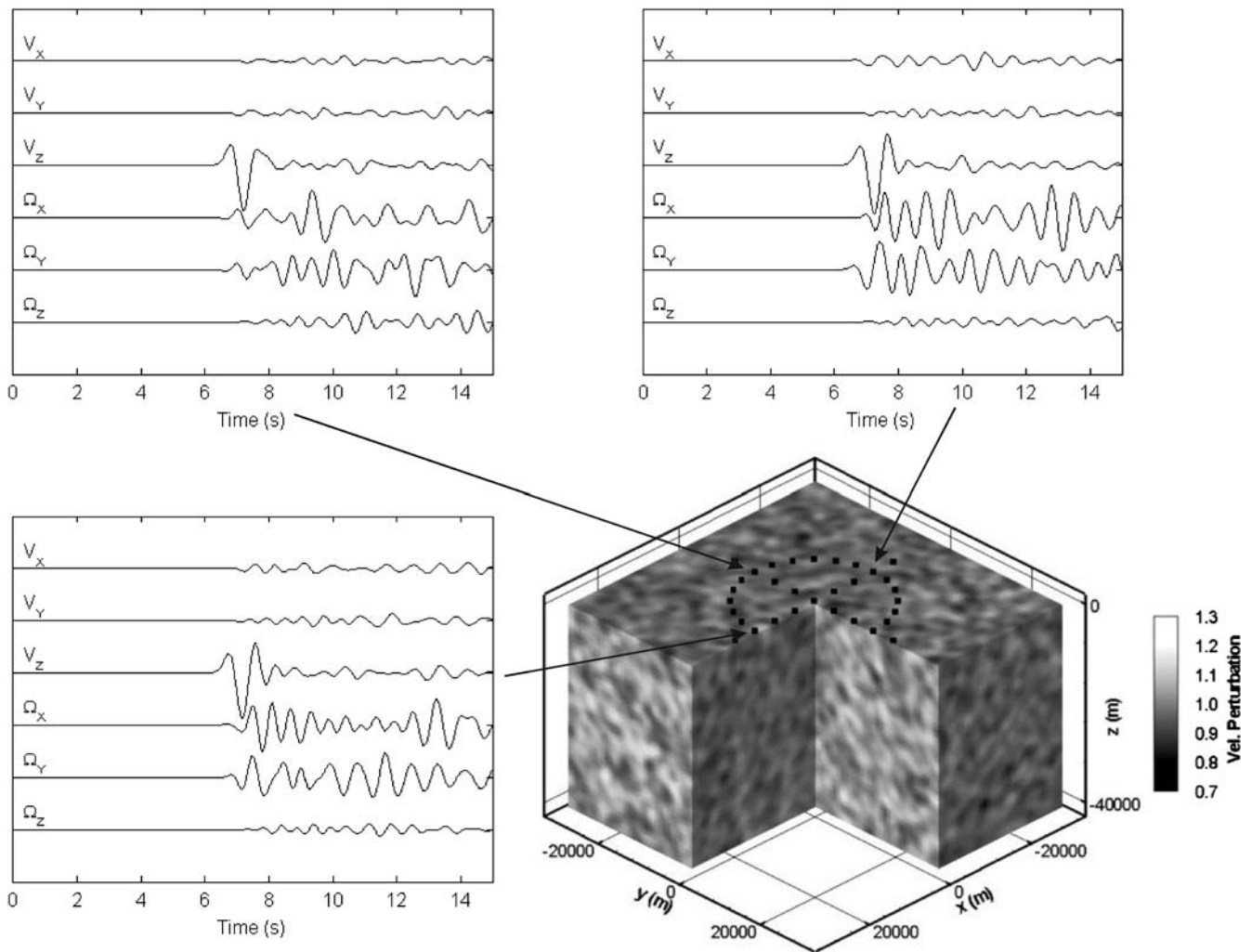|	
Mesh type	Hexahedral
Element edge length	950 m
Total number of elements	176128
Polynomial order inside elements	4
Number of processors	64
Length of seismograms	60 sec
Boundary conditions	Free surface (top), inflow (bottom), periodic (sides)
Average time step	8.13008×10^{-3} sec
Run time per simulation	~2 hours

Figure 10. Schematic illustration of a 3D Von Kármán random medium used in this study (correlation length $a = 2000$ m, root mean square perturbation of V_S is 6.51%) and six-component seismograms obtained at three different receivers for a plane P wave propagating upward (in a vertical direction) from the bottom of the model. For each set of translational velocities (V_x, V_y, and V_z) or rotation rates (Ω_x, Ω_y, and Ω_z) amplitudes are scaled.

ratio being about 1.8×10^{-8} (Fig. 13b, bottom panel, the section between about 7340 and 7365 sec).

These ratios are calculated for windows of varying duration beginning at the onset of the *P* wave. The results for four typical events are shown in Figure 14 with the lengths of the windows given by the horizontal axis. The figure shows that after the window length reaches 15 sec the energy ratios for different events attain a quite stable value of about $1.1–2.6 \times 10^{-8}$, almost the same value that we obtained with sliding windows before. This stable value remains in the range of window length from 15 to 35 sec for all four events (bottom panel). We return to the modeling part to investigate which scattering parameters are compatible with the observed energy ratio.

We use a window of 15 sec length beginning at the onset of the *P*-wave synthetics. For each pair of scattering parameters (a velocity perturbation and a correlation length), we obtain a value of the energy ratio, averaged through

all 24 receivers in circular configuration (Fig. 10). Initially, we take a fixed correlation length of 2000 m and calculate the average energy ratios as a function of velocity perturbation. The results are shown as a black curve in Figure 15. As expected, the energy ratio increases as we increase the perturbation. The curve shows a nonlinear behavior, with the slope decreasing as the perturbation increases. Similarly, we can calculate the average energy ratio as a function of correlation length at some fixed values of velocity perturbation. We cover a range of correlation lengths from 1000 up to 15,000 m and fixed perturbation values of 4.8%, 6.1%, and 8%. The results are plotted as squares in Figure 15 and strongly suggest that for our model geometry the energy ratio is much more sensitive to the velocity perturbation than to the correlation length.

We can finally try to explain the origin of the $1.1–2.6 \times 10^8$ value for the energy ratio consistently observed at Wettzell. Although the value of the correlation length, that is, the
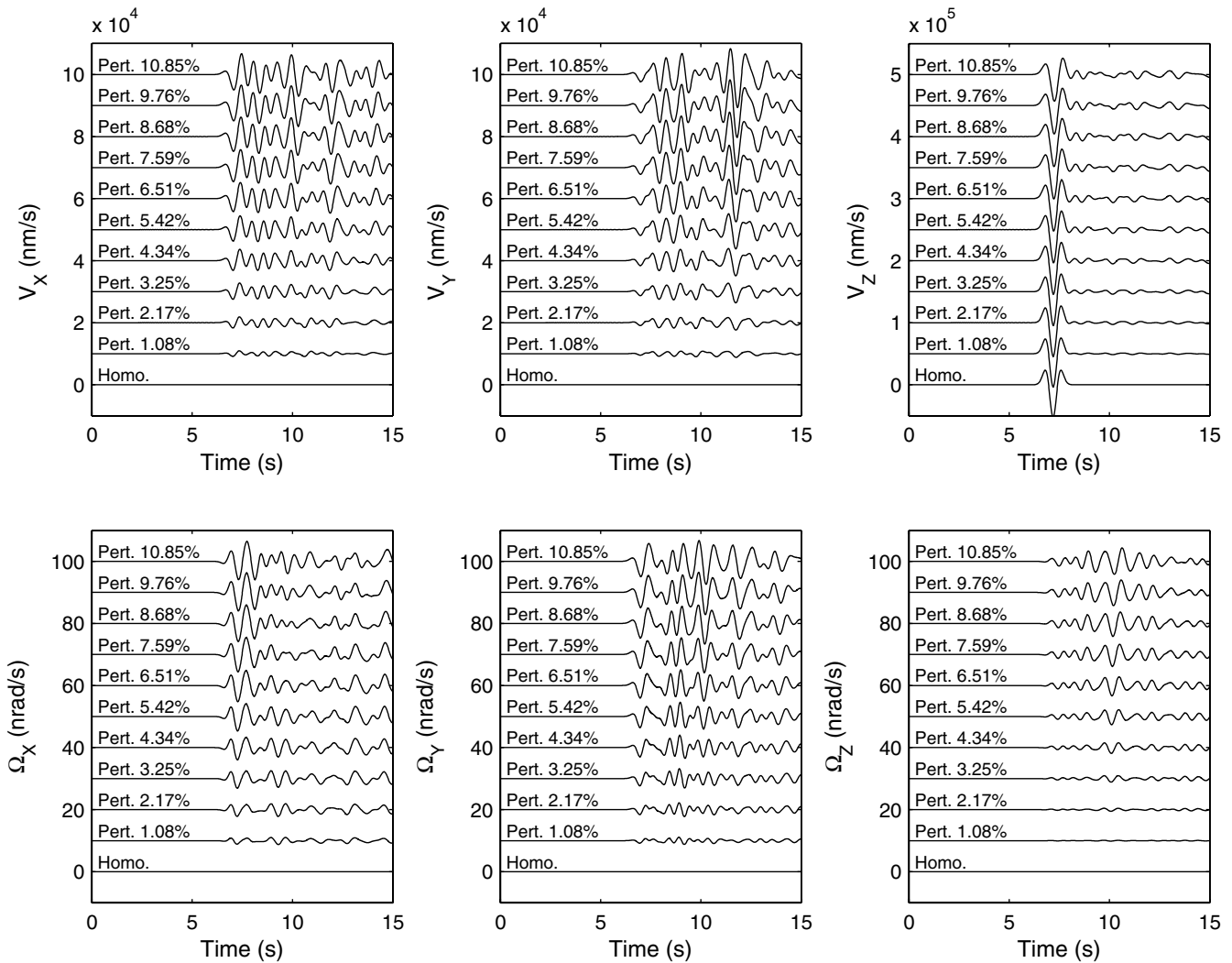
Figure 11. Variations of six-component seismograms obtained at one receiver as a function of velocity perturbation of the random medium (correlation length is fixed at 2000 m) when a plane *P* wave propagates upward (in a vertical direction) from the bottom of the model.

size of the scatterers, cannot be constrained, our simulations show that the observed range of energy ratios (as can be seen in the gray area of Fig. 15) are compatible with crust models containing velocity perturbation values ranging from 4.8% to 6.5%.

Discussions and Conclusions

The first observations of the ring laser rotational signals in the *P* coda of teleseismic events were reported by Igel *et al.* (2007). However, the origin of the *P*-coda rotations was unclear. The main goals of this study are (1) to characterize the observations of *P*-coda rotations in detail and (2) to model the observations in terms of *P-SH* scattering.

The observations presented in this article indicate that the energies of the *P*-coda rotations are predominant at high frequencies, come from many different directions, and increase in time slower than that of the energy in the verti-

cal component of translation. The distribution of cross-correlation coefficients between rotation rate and transverse acceleration as a function of time and cutoff period demonstrates an effective tool to separate direct *S* waves from the scattering field. The explanation for the *P*-coda rotations by *P-SH* scattering is affirmed by the simulation results shown in this study. Under the assumption of a random crustal medium, rotational signals in the *P* coda can be generated efficiently.

The phenomenon of energy equipartitioning into *P* and *S* waves studied by Shapiro *et al.* (2000) and Hennino *et al.* (2001) is considered as the principle of multiple scattering. Our study provides further evidence of energy equipartition, indicated by the stabilization of the ratio of energies of vertical rotation rate and vertical translation velocity after the onset of the *P* wave. This stable energy ratio allows us to constrain the velocity perturbation of the random crustal model. Under the assumption of a Von Kármán random me-
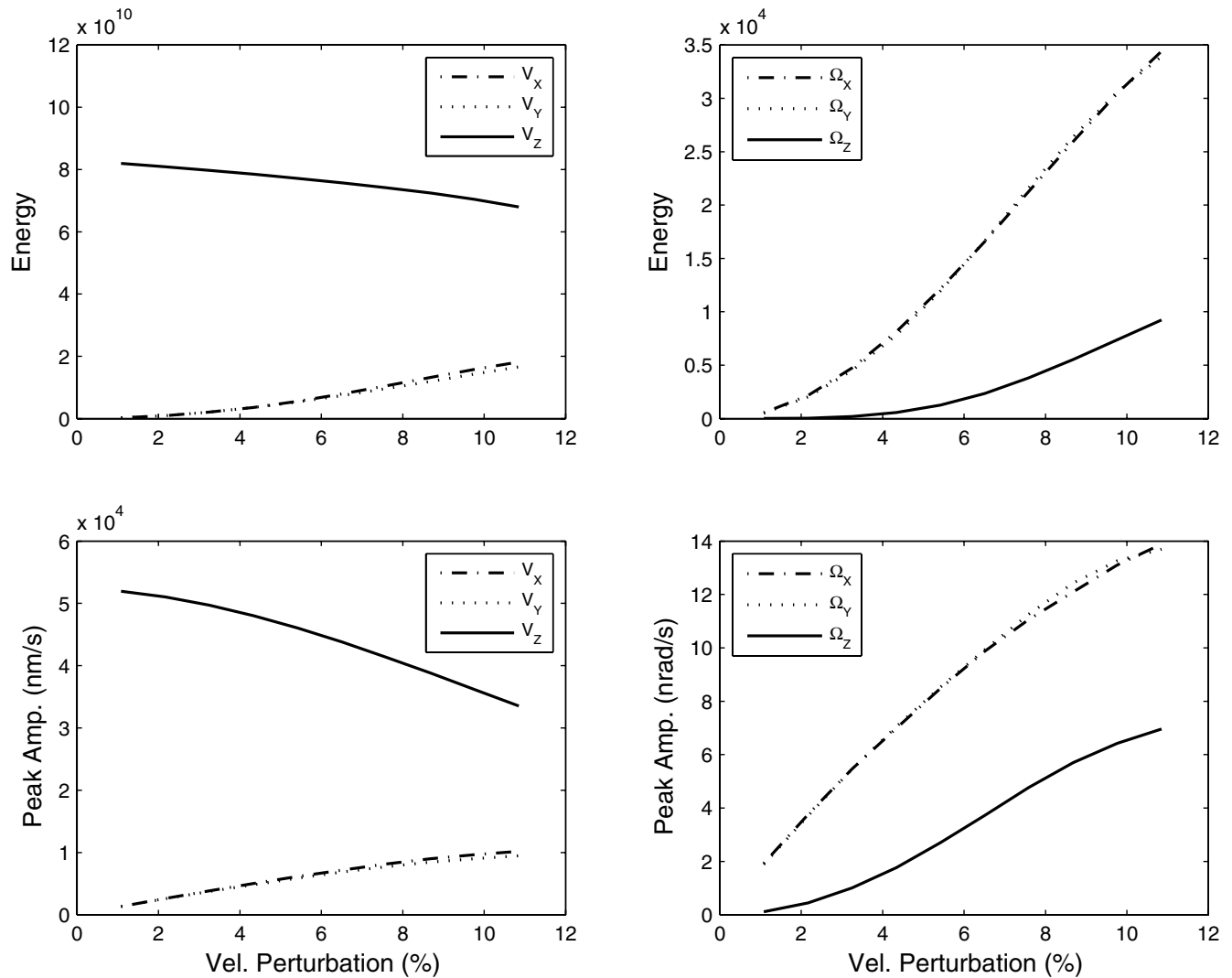
Figure 12.   Variations of (the average values of) energy and peak amplitude of each translation and rotation component (calculated from 21 sec seismograms of 24 receivers distributed regularly around a circle of radius 15 km from the center point at the surface of the model, Fig. 10) as a function of velocity perturbation of the random medium (correlation length is fixed to 2000 m) when a plane *P* wave propagates upward (in a vertical direction) from the bottom of the model.

dium, we obtain velocity perturbation values ranging from 4.8% to 6.5% for the Wettzell area.

In summary, it can be concluded that *P-SH* scattering in the crust can explain the *P*-coda observations and rotation sensors offers a direct measurement of *SH* energy and thus may help understanding the partitioning of *P* and *S* energy. The contributions of topography scattering and anisotropy in the observed *P*-coda rotations remain open issues and will be addressed in the future.

Data and Resources

The observed seismograms of the period 2003–2004 used in this study were provided by the Geophysics Section, Ludwig Maximilians University (LMU) Munich and published by Igel *et al.*, 2007. The seismograms of the events that occurred after September 2007 can be obtained from the WebDC-Integrated Seismological Data Portal at http://www.webdc.eu/arclink/query?sesskey=0841ed49 (last accessed March 2008).
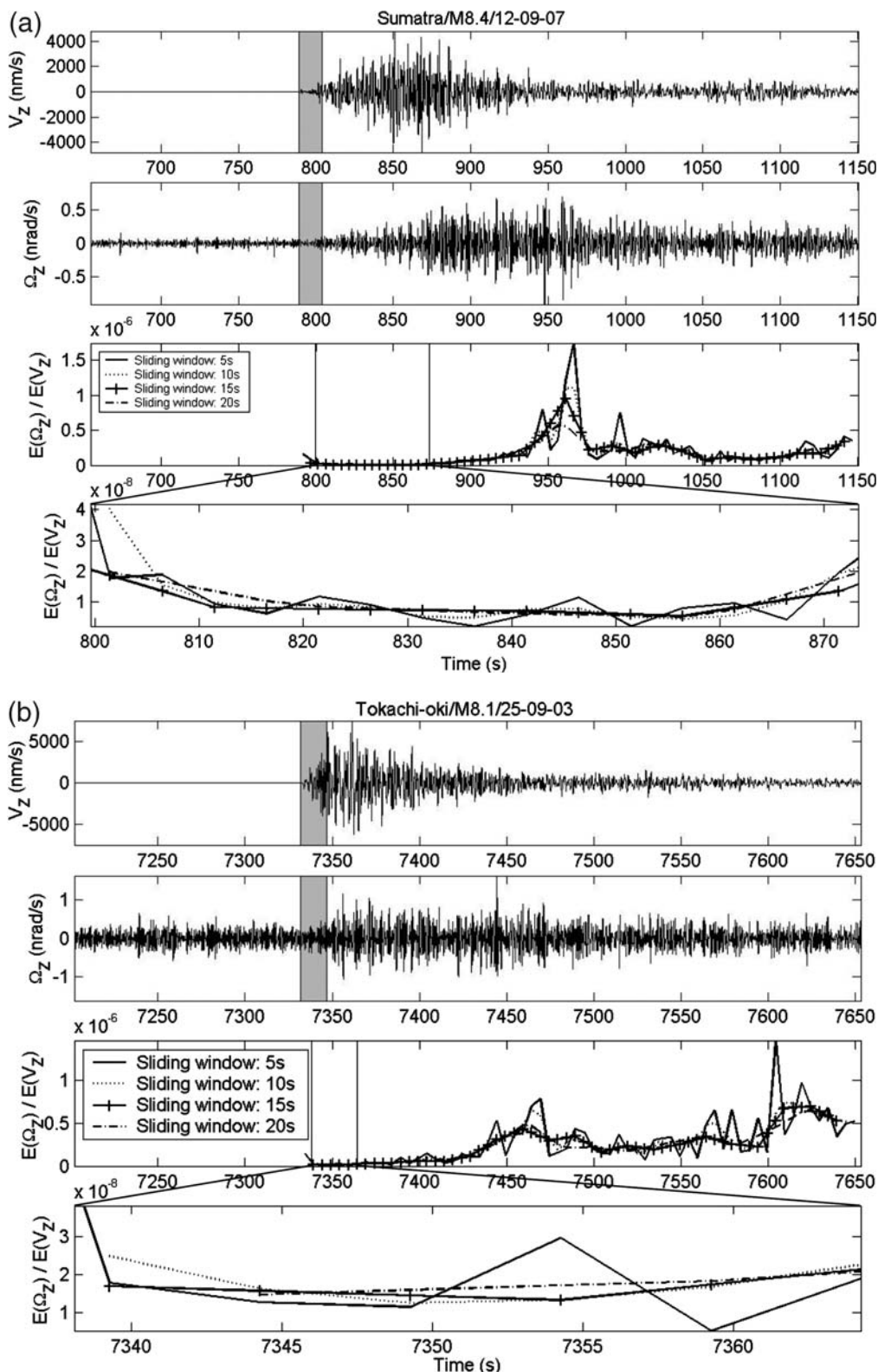
Acknowledgments

Figure 13. (a) Two top traces: vertical components of velocity and rotation rate, respectively, in the P coda of the 12 September 2007 M 8.4 Sumatra event after band-pass filtering between 0.5 and 1.5 sec. Two bottom traces: ratio between the energy of rotation rate and energy of vertical velocity calculated for time windows (illustrated by the vertical gray bands in the top traces) of different lengths, starting from the onset of P and sliding along the time series up to the end of the P coda. (b) Two top traces: vertical components of velocity and rotation rate, respectively, in the P coda of the 25 September 2003 M 8.1 Tokachi-oki event after band-pass filtering between 0.5 and 1.5 sec. Two bottom traces: ratio between the energy of rotation rate and energy of vertical velocity calculated for time windows (illustrated by the vertical gray bands in the top two traces) of different lengths, starting from the onset of P and sliding along the time series up to the end of the P coda.
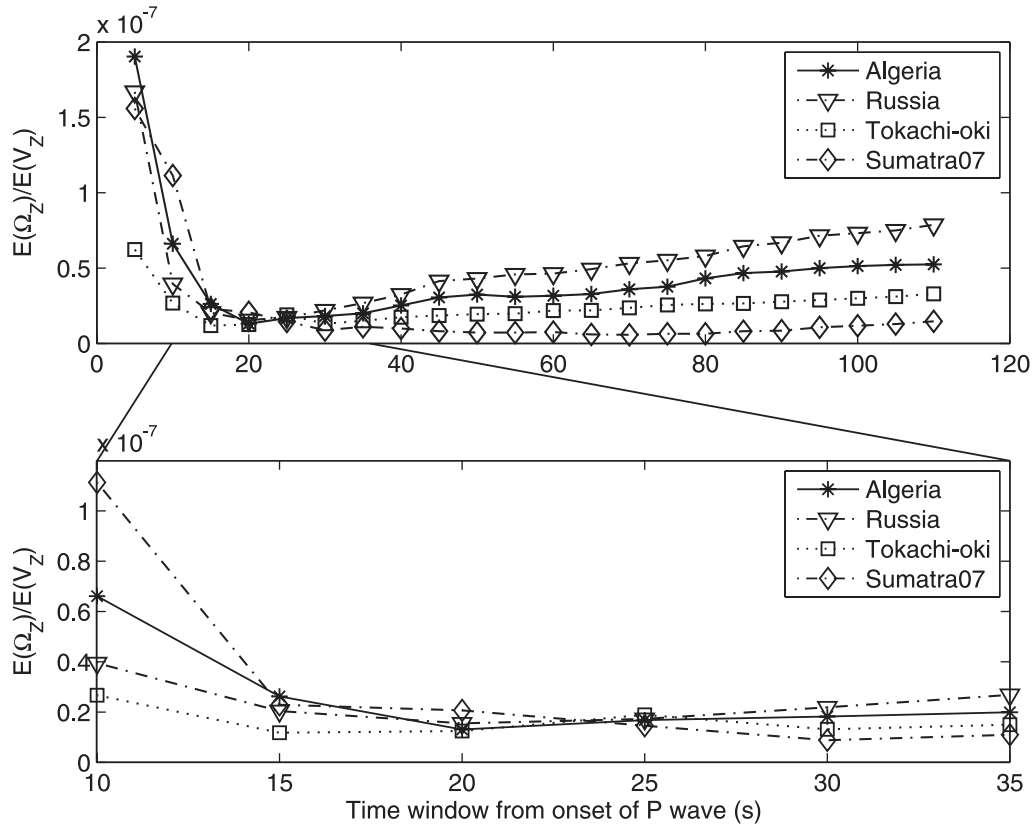
Figure 14. Ratios between the energy of rotation rate and energy of vertical velocity in typical events calculated for different time windows. All the time windows start at the onset of direct *P* waves, and their lengths are given by the horizontal axis.
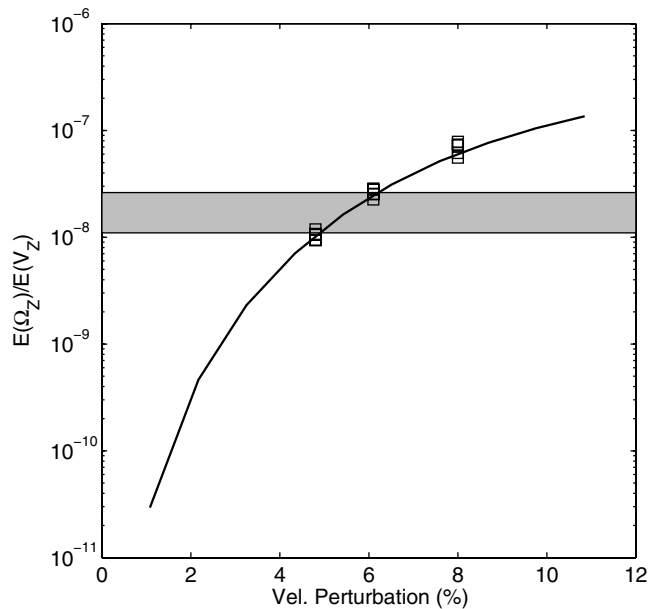
References

Figure 15. Comparison of observed and simulated energy ratios. Black curve, the (average) energy ratio as a function of velocity perturbation calculated from simulated seismograms (correlation length fixed at 2000 m); squares, the (average) energy ratio as a function of correlation length (from 1000 up to 15,000 m) obtained from simulations; Horizontal gray band, range of the energy ratios obtained from observations.

Aki, K., and P. G. Richards (2002). *Quantitative Seismology* Second Ed., University Science Books, Sausalito, California.

Bassin, C., G. Laske, and G. Masters (2000). The current limits of resolution for surface wave tomography in North America, *EOS Trans. AGU* **81,** F897.

Cochard, A., H. Igel, B. Schuberth, W. Suryanto, A. Velikoseltsev, U. Schreiber, J. Wassermann, F. Scherbaum, and D. Vollmer (2006). Rotational motions in seismology: theory, observations, simulation, in *Earthquake Source Asymmetry, Structural Media and Rotation Effects*, R. Teisseyre, M. Takeo, and E. Majewski (Editors), Springer-Verlag, New York, 391–412.

Dumbser, M., and M. Käser (2006). An arbitrary high order discontinuous Galerkin method for elastic waves on unstructured meshes II: the three-dimensional isotropic case, *Geophys. J. Int.* **167,** no. 1, 319–336, doi 10.1111/j.1365-246X.2006.03120.x.

Fichtner, A., and H. Igel (2009). Sensitivity densities for rotational ground-motion measurements, *Bull. Seismol. Soc. Am.* **99,** no. 2B, 1302–1314.

Graizer, V. M. (2005). Effect of tilt on strong motion data processing, *Soil Dyn. Earthq. Eng.* **25,** 197–204.

Graizer, V. M. (2006). Equation of pendulum motion including rotations and its implications to the strong-ground motion, in *Earthquake Source Asymmetry, Structural Media and Rotation Effects*, R. Teisseyre, M. Takeo, and E. Majewski (Editors), Springer-Verlag, New York, 471–491.

Hennino, R., N. Trégourès, N. M. Shapiro, L. Margerin, M. Campillo, B. A. van Tiggelen, and R. L. Weaver (2001). Observation of equipartition of seismic waves, *Phys. Rev. Lett.* **86,** 3447–3450, doi 10.1103/PhysRevLett.86.3447.

Igel, H., A. Cochard, J. Wassermann, A. Flaws, U. Schreiber, A. Velikoseltsev, and D. N. Pham (2007). Broadband observations of earthquake

induced rotational ground motions, *Geophys. J. Int.* **168,** 182–196, doi 10.1111/j.1365-246X.2006.03146x.

Igel, H., K. U. Schreiber, A. Flaws, B. Schuberth, A. Velikoseltsev, and A. Cochard (2005). Rotational motions induced by the *M* 8.1 Tokachi-oki earthquake, September 25, 2003, *Geophys. Res. Lett.* **32,** L08309, doi 10.1029/2004GL022336.

Klimeš, L. (2002). Correlation functions of random media, *Pure Appl. Geophys.* **159,** 1811–1831.

Li, H., L. Sun, and S. Wang (2001). Improved approach for obtaining rotational components of seismic motion, *Transactions, SmiRT* **16,** 1–8.

Li, H., L. Sun, and S. Wang (2002). Frequency dispersion characteristics of phase velocities in surface wave for rotational components of seismic motion, *J. Sound Vib.* **258,** no. 5, 815–827.

McLeod, D. P., G. E. Stedman, T. H. Webb, and U. Schreiber (1998). Comparison of standard and ring laser rotational seismograms, *Bull. Seismol. Soc. Am.* **88,** 1495–1503.

Pancha, A., T. H. Webb, G. E. Stedman, D. P. McLeod, and U. Schreiber (2000). Ring laser detection of rotations from teleseismic waves, *Geophys. Res. Lett.* **27,** 3553–3556.

Pham, N. D., H. Igel, J. Wassermann, A. Cochard, and U. Schreiber (2009). The effects of tilt on interferometric rotation sensors, *Bull. Seismol. Soc. Am.* **99,** no. 2B, 1352–1365.

Pillet, R., and J. Virieux (2007). The effects of seismic rotations on inertial sensors, *Geophys. J. Int.* **171,** no. 3, 1314–1323, doi 10.1111/j.1365-246X.2007.03617.x.

Schreiber, U., H. Igel, A. Cochard, A. Velikoseltsev, A. Flaws, B. Schuberth, W. Drewitz, and F. Müller (2005). The GEOsensor project: a new observable for seismology, in *Observation of the System Earth from Space*, J. Flury, R. Rummel, C. Reigber, M. Rothacher, G. Boedecker, and U. Schreiber (Editors), Springer, Berlin, 427–443.

Schreiber, U., G. E. Stedman, H. Igel, and A. Flaws (2006). Ring laser gyroscopes as rotation sensors for seismic wave studies, in *Earthquake Source Asymmetry, Structural Media and Rotation Effects*, R. Teisseyre, M. Takeo, and E. Majewski (Editors), Springer-Verlag, New York, 377–390.

Shapiro, N. M., M. Campillo, L. Margerin, S. K. Singh, V. Kostoglodov, and J. Pacheco (2000). The energy partitioning and the diffusive character of the seismic coda, *Bull. Seismol. Soc. Am.* **90,** 655–665.

Stein, S., and M. Wysession (2003). *An Introduction to Seismology, Earthquake, and Earth Structure*, Blackwell Publishing, Oxford.

Takeo, M. (1998). Ground rotational motions recorded in near-source region of earthquakes, *Geophys. Res. Lett.* **25,** 789–792.

Takeo, M., and H. M. Ito (1997). What can be learned from rotational motions excited by earthquakes?, *Geophys. J. Int.* **129,** 319–329.

Trifunac, M. D., and M. I. Todorovska (2001). A note on the usable dynamic range of accelerographs recording translation, *Soil Dyn. Earthq. Eng.* **21,** no. 4, 275–286.

Geophysics Section
Department of Earth and Environmental Sciences
Ludwig Maximilians Universität
Theresienstrasse 41
D-80333 München, Germany
nguyen@geophysik.uni-muenchen.de
heiner.igel@lmu.de
igel@geophysik.uni-muenchen.de
heiner.igel@geophysik.uni-muenchen.de
martin.kaeser@geophysik.uni-muenchen.de
        (N.D.P., H.I., M.K., J.d.)

Geophysical Observatory
Department of Earth and Environmental Sciences
Ludwig Maximilians Universität
Ludwigshöhe 8
82256 Fürstenfeldbruck, Germany
joachim.wassermann@geophysik.uni-muenchen.de
        (J.W.)

Forschungseinrichtung Satellitengeodäsie
Technical University Munich
Fundamentalstation Wettzell, Sackenriederstrasse 25
D-93444 Kötzting, Germany
schreiber@wettzell.ifag.de
        (U.S.)